On the Design of Yaw Rate Control via Variable Front-to-Total Anti-Roll Moment Distribution

Marco Ricco, Mattia Zanchetta [ID], Giovanni Cardolini Rizzo, Davide Tavernini [ID], Aldo Sorniotti [ID], *Member, IEEE*, Christoforos Chatzikomis, Mauro Velardocchia, Marc Geraerts, and Miguel Dhaens

Abstract—In vehicle dynamics, yaw rate control is used to improve the cornering response in steady-state and transient conditions. This can be achieved through an appropriate anti-roll moment distribution between the front and rear axles of a vehicle with controllable suspension actuators. Such control action alters the load transfer distribution, which in turn provokes a lateral tire force variation. With respect to the extensive set of papers from the literature discussing yaw rate tracking through active suspension control, this study presents: i) A detailed analysis of the effect of the load transfer on the lateral axle force and cornering stiffness; ii) A novel linearized single-track vehicle model formulation for control system design, based on the results in i); and iii) An optimization-based routine for the design of the non-linear feedforward contribution of the control action. The resulting feedforward-feedback controller is assessed through: a) Simulations with an experimentally validated model of a vehicle with active anti-roll bars (case study 1); and b) Experimental tests on a vehicle prototype with an active suspension system (case study 2).

Index Terms—Anti-roll moment distribution control, load transfer, linearized model, quasi-static model, yaw rate control, feedforward, feedback.

I. INTRODUCTION

CHASSIS control systems use yaw rate and sideslip angle control to enhance the steady-state and transient cornering response of a vehicle. The target is to vary the level of vehicle understeer in quasi-steady-state conditions, and to increase yaw and sideslip damping during transients. In conventional production cars, the control of yaw rate and sideslip angle is commonly achieved through direct yaw moment control, which is actuated by the friction brakes only in emergency conditions [1], [2]. Continuous direct yaw moment control is performed in vehicles with torque-vectoring systems, e.g., with drivetrain set-ups including torque-vectoring devices or multiple electric motors [3]–[5]. However, such configurations require relatively advanced and expensive powertrain hardware. A significant number of papers discusses continuously active controllers for vehicles with multiple actuators. For example, Nagai *et al.* propose yaw rate and sideslip control through an integrated rear-wheel-steering and direct yaw moment controller, capable of improving vehicle response both in normal driving conditions and at the limit of handling [6].

An alternative method for achieving similar objectives is represented by active suspension control [7]–[9], either implemented through individual actuators on each vehicle corner, or active anti-roll bars [10]–[12]. Among other variables, such systems control the anti-roll moment distribution between the front and rear axles. This varies the lateral axle forces, slip angles, and the level of vehicle understeer [13]–[17]. An analysis of the potential vehicle dynamics benefits of active suspension systems is included in [18]. Various papers, e.g., [19]–[20], compare the handling control authority of active suspension control, four-wheel-steering / active steering control and direct yaw moment control, reaching the conclusion that active suspensions can be rather effective in proximity of the cornering limit.

Extensive literature discusses ride comfort control, body motion control (roll and pitch control [21]–[23]) as well as yaw rate and sideslip angle control through active and semi-active suspensions, either on their own or integrated with other chassis control systems. For example, Cooper *et al.* [24] use an empirically tuned proportional integral derivative (PID) controller. References [25]–[27] present predictive controllers, linear quadratic regulators (LQRs) and linear quadratic Gaussian (LQG) controllers, which are based on the minimization of specific optimality criteria. H_∞ controllers are often used to provide system robustness, given the significant uncertainties of the models for control system design [28]–[30]. Many suspension studies apply sliding mode controllers [31]–[34], which can compensate uncertainties and disturbances. Several roll and pitch control implementations include feedforward components, e.g., directly based on driver inputs, cooperating with feedback contributions [35]–[38]; however, to the best of the authors' knowledge, there is lack of studies on feedforward suspension control for achieving a desired cornering response. References [39]–[44] apply elements of fuzzy control to vehicle chassis systems including controllable suspensions.

On the topic of model-based suspension control design, [7] states that "as the effect of the lateral load transfer on the

M. Ricco, M. Zanchetta, G. C. Rizzo, D. Tavernini, A. Sorniotti, and C. Chatzikomis are with the University of Surrey, GU2 7XH Guildford, U.K. (e-mail: m.ricco@surrey.ac.uk; m.zanchetta@surrey.ac.uk; g.cardolini@surrey.ac.uk; d.tavernini@surrey.ac.uk; a.sorniotti@surrey.ac.uk; c.chatzikomis@surrey.ac.uk).

M. Velardocchia is with the Politecnico di Torino, 10129 Turin, Italy (e-mail: mauro.velardocchia@polito.it).

M. Geraerts and M. Dhaens are with Tenneco Automotive Europe BVBA, 3800 Sint-Truiden, Belgium (e-mail: Mgeraerts@Tenneco.com; Mdhaens@Tenneco.com).

lateral/directional dynamics in itself is strongly nonlinear, it is difficult to derive the control law by using the fully analytical method. Therefore, this paper concentrates on computer simulation of vehicle response" for the design of the controller. On the other hand, the model for control system design mostly adopted in the literature (see [8] and [25]) considers a parabolic variation of tire cornering stiffness with vertical load. In such formulation, the increased axle load transfer caused by an active anti-roll moment always provokes a decrease of the axle cornering stiffness. A slightly more advanced approach is presented in [13], which uses a non-linear relationship between slip angle, load transfer and lateral axle force. Nevertheless, such methods are rather simplistic, and their limitations need a detailed assessment.

Although in the literature the front-to-total anti-roll moment distribution formulations for yaw rate tracking are based on feedback control, the recent industrial trend for continuously active chassis controllers is to have important feedforward contributions. These can generate a vehicle response that is very different from that of the passive vehicle, but at the same time they convey an impression of 'natural' behavior, e.g., as if the modified cornering characteristics were achieved through an appropriate hardware set-up. In fact, the feedforward contribution is not affected by the signal noise of the inertial measurement unit, which is a typical practical issue of continuously active feedback control.

To cover such knowledge gap, this paper presents a front-to-total anti-roll moment distribution controller, and provides the following novel contributions:

- The detailed analysis of the effect of the load transfer variation on the lateral axle force and cornering stiffness.
- An optimization routine based on a quasi-static vehicle model for the design of the non-linear feedforward contribution, to achieve an assigned set of reference understeer characteristics.
- The design of the feedback contribution through a novel linearized single-track model formulation, considering the effect of the front-to-total anti-roll moment distribution on the cornering response.

The performance of the controller is assessed through: a) Simulations with an experimentally validated non-linear model of a sport utility vehicle (SUV) with active anti-roll bars (case study 1); and b) Preliminary experimental tests on a second SUV with active suspension actuators (case study 2).

II. EFFECT OF LATERAL LOAD TRANSFER ON LATERAL AXLE FORCE

This section uses the Pacejka magic formula (MF [45], version 5.2) tire model of the case study 1 SUV. Fig. 1 is the lateral force characteristic for a single front tire F_y, as a function of slip angle α, for six values of vertical load F_z, with slip ratio σ_x and camber angle γ equal to 0. All curves exhibit an almost linear behavior for small slip angles (note that the tire forces are not exactly zero at zero slip angle because of the effects of conicity and ply steer). As α increases, the characteristics become non-linear and experience a progressive reduction of their gradient, which is negative once the lateral force capability is saturated.
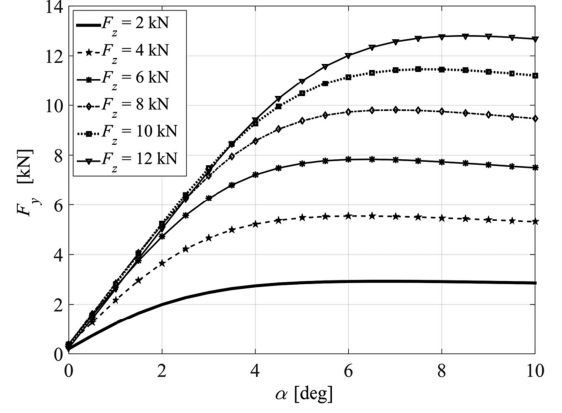

Fig. 1.   Case study 1: front lateral tire force (F_y) characteristic as a function of slip angle (α), for different vertical loads (F_z).

Tire saturation occurs at larger slip angles if the vertical load is high.

Active suspension systems allow the control of the anti-roll moment contribution $M_{AR,Act,i}$, applied to each axle by the suspension actuators, where the subscript $i = F, R$ refers to the front or rear axle. $M_{AR,Act,i}$ counteracts the effect of the inertial force in cornering and is proportional to the lateral load transfer $\Delta F_{z,i}$, i.e., the vertical tire load variation with respect to the condition of straight line operation. In a first approximation, $\Delta F_{z,i}$ is given by [46], [47]:

$$\Delta F_{z,i} = \frac{ma_y\,[l - a_i]\,d_i}{lt_i} + \frac{M_{AR,i}}{t_i} \qquad (1)$$

where m is the vehicle mass; a_y is the lateral acceleration; a_i is the semi-wheelbase, i.e., the distance between the axle and the center of gravity in longitudinal direction; l is the wheelbase; d_i is the roll center height; t_i is the track width; and $M_{AR,i}$ is the sum of the passive and active anti-roll moment contributions. This means that $M_{AR,i} = M_{AR,PS,i} + M_{AR,PD,i} + M_{AR,Act,i}$, where $M_{AR,PS,i}$ is the anti-roll moment associated with the passive springs and anti-roll bars; and $M_{AR,PD,i}$ is the anti-roll moment caused by the damping contribution of the passive components.

Based on (1), the modeling and analysis of the effect of $\Delta F_{z,i}$ on the lateral axle force $F_{y,i}$ is crucial to the correct design of front-to-total anti-roll moment distribution controllers. To this purpose, under the reasonable hypotheses of small steering angles and parallel direction of the lateral forces of the two tires on the same axle, Fig. 2 plots the front axle force $F_{y,F}$, i.e., the sum of the individual tire cornering forces from the MF model, as a function of the front axle slip angle, α_F, and load transfer, $\Delta F_{z,F}$:

$$F_{y,F} = F_y\left(\alpha_F; F_{z,F,0} + \Delta F_{z,F}; \sigma_{x,F} = 0; \gamma_{F,Out}\right)$$
$$+ F_y\left(\alpha_F; F_{z,F,0} - \Delta F_{z,F}; \sigma_{x,F} = 0; \gamma_{F,In}\right) \quad (2)$$

where $F_{z,F,0}$ is the static value of front tire load, i.e., for the condition of straight line operation; and $\gamma_{F,Out}$ and $\gamma_{F,In}$ are the camber angles of the outer and inner tire. Given the general nature of this preliminary discussion and the verified very marginal influence of camber angle for the specific applications,
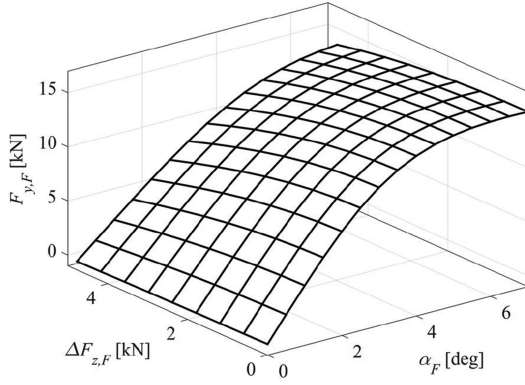
Fig. 2.   Case study 1: lateral force of the front axle ($F_{y,F}$) as a function of slip angle (α_F) and lateral load transfer ($\Delta F_{z,F}$).
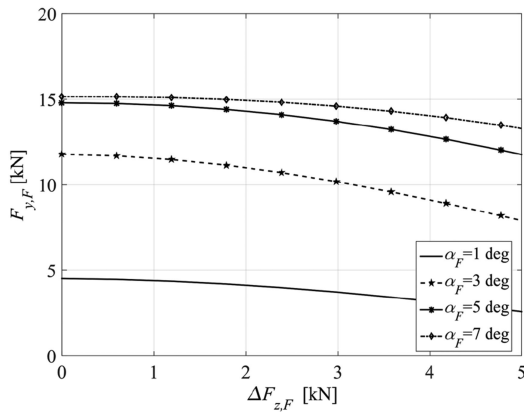

Fig. 3.   Case study 1: lateral force of the front axle ($F_{y,F}$) as a function of the lateral load transfer ($\Delta F_{z,F}$) for set values of α_F.

$\gamma_{F,Out}$ and $\gamma_{F,In}$ are assumed to be zero (they will not be so in the vehicle model implementations of the following sections). The round brackets '()' in (2) and in the remainder are used to indicate the argument of a function.

The lateral axle force in Fig. 2 has a similar behavior to the lateral force of the single tire (see Fig. 1), with respect to slip angle. On the other hand, an increase of $\Delta F_{z,F}$ causes a non-linear reduction of $F_{y,F}$, as shown in Fig. 2 and more clearly in Fig. 3, obtained by bisecting the three-dimensional plot of Fig. 2 at different α_F values.

The models commonly adopted for the design of the front-to-total anti-roll moment distribution controllers (see [8] and [25]) consider the lateral axle force as the product of the axle cornering stiffness C_i, expressed as a function of $\Delta F_{z,i}$, by the respective slip angle α_i.

In this study C_i is defined as the partial derivative of the lateral axle force with respect to slip angle, calculated at a nominal slip angle $\alpha_{i,0}$, and a load transfer $\Delta F_{z,i}$. In practice, C_i is computed as an incremental ratio:

$$C_i = \frac{\partial F_{y,i}}{\partial \alpha} (\alpha_{i,0}; \Delta F_{z,i})$$

$$\approx \frac{F_{y,i} (\alpha_{i,0} + \Delta\alpha; \Delta F_{z,i}) - F_{y,i} (\alpha_{i,0}; \Delta F_{z,i})}{\Delta\alpha} \quad (3)$$

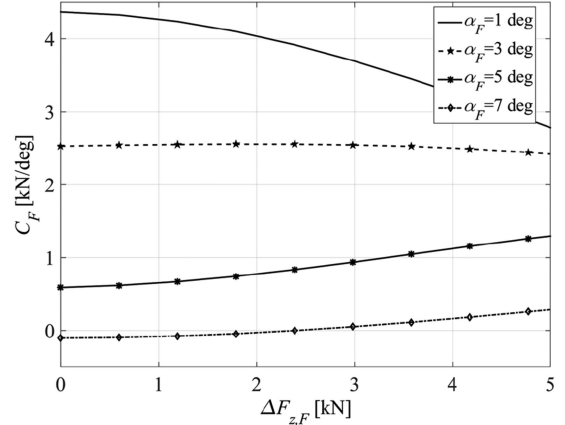where $\Delta\alpha$ is the slip angle increment.

Fig. 4.   Case study 1: front axle cornering stiffness (C_F) as a function of the lateral load transfer ($\Delta F_{z,F}$) for set values of α_F.

Fig. 4 shows the results of the calculation for the front axle of the SUV, at four values of $\alpha_{F,0}$, for $\Delta\alpha = 0.1$ deg. Interestingly C_F decreases with $\Delta F_{z,F}$ only for $\alpha_{F,0} = 1$ deg, while at $\alpha_{F,0} = 3$ deg it is approximately constant, and for $\alpha_{F,0} = 5$ deg and $\alpha_{F,0} = 7$ deg C_F increases with $\Delta F_{z,F}$. The increase of C_F is caused by the increase of cornering stiffness of the laden tire, as the slip angle at which tire saturation occurs increases with vertical load (see Fig. 1).

The important conclusion of the analysis of Figs. 2–4 is that the lateral axle force always decreases with the lateral load transfer, but the cornering stiffness can decrease or increase. In particular, the cornering stiffness increases with the load transfer for medium-high values of slip angle, i.e., for medium-high lateral accelerations. Similar trend was verified for other realistic tire parameters. Such observation is in contrast with the modeling approximation usually adopted in the literature in the control system design phase (see [8] and [25]) and justifies the development of a novel linearized formulation of the lateral axle force.

III. LINEARIZED AXLE FORCE FORMULATION

A. Simplified Axle Force Formulation (Model A)

A realistic yet simple linearized lateral axle force model is required for the design of the front-to-total anti-roll moment distribution in the frequency domain. As the linearization of a conventional non-linear tire model, such as the MF, would bring a rather complex formulation, a specific method is developed in this study.

Fig. 5 illustrates the principle of the adopted linearization approach, called Model A in the remainder. For a linearization point defined by the slip angle $\alpha_{i,0}$ and the corresponding lateral axle force $F_{y,i,Lin,0}$, the axle force at the nominal load transfer $\Delta F_{z,i,0}$, is expressed by a line tangent to the axle force characteristic in $(\alpha_{i,0}; F_{y,i,Lin,0})$. The angular coefficient is the nominal value of the axle cornering stiffness $C_{i,0}$. If for the same $\alpha_{i,0}$ the load transfer is varied from $\Delta F_{z,i,0}$ to $\Delta F_{z,i}$, both the force at the linearization point and cornering
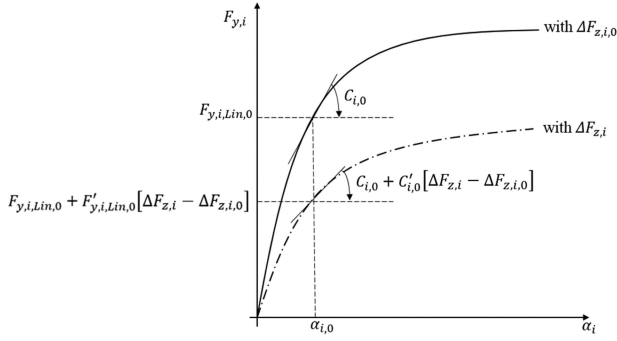
Fig. 5. Lateral axle force linearization according to Model A.

a_y [m/s^2]	$F_{y,F,0}$ [N]	$F_{y,F,ILT,0}$ [N]	$\Delta F_{y,Mx,0}$ [N]	$\Delta F_{y,Mx,-0.5}$ [N]	$\Delta F_{y,Mx,+0.5}$ [N]	$\Delta F_{y,0,\%}$ [%]	$\Delta F_{y,-0.5,\%}$ [%]	$\Delta F_{y,+0.5,\%}$ [%]
MF								
3	3734	3619	115	48	178	-	-	-
6	7664	7217	447	364	505	-	-	-
9	11589	10946	643	611	611	-	-	-
MODEL A								
3	3734	3628	106	42	174	7.82	12.50	2.23
6	7664	7226	438	366	510	2.01	0.55	0.99
9	11589	10947	642	673	611	0.16	0.75	0
MODEL B								
3	3757	3638	119	49	189	3.48	2.08	6.18
6	8051	7537	514	392	637	14.99	7.69	26.14
9	14138	12656	1482	1327	1636	130.48	98.65	167.76
MODEL C								
3	3734	3734	0	66	66	100	37.50	62.92
6	7664	7664	0	72	72	100	80.22	85.74
9	11589	11589	0	31	31	100	95.36	94.93

stiffness change, and their new values are indicated as $F_{y,i,Lin}$ and C_i.

The lateral axle force $F_{y,i}$ at a generic α_i is expressed as:

$$F_{y,i} \approx F_{y,i,Lin} + C_i\left[\alpha_i - \alpha_{i,0}\right] \qquad (4)$$

Based on Fig. 5, the cornering stiffness and lateral force at the linearization point are functions of the lateral load transfer, i.e., $C_i = C_i(\Delta F_{z,i})$ and $F_{y,i,Lin} = F_{y,i,Lin}(\Delta F_{z,i})$. With a first order Taylor series expansion, it is:

$$C_i \approx C_{i,0} + C'_{i,0}\left[\Delta F_{z,i} - \Delta F_{z,i,0}\right] \qquad (5)$$

where $C'_{i,0}$ is the cornering stiffness gradient with respect to the load transfer, calculated at $\Delta F_{z,i,0}$. Similarly, the lateral force at $\alpha_{i,0}$ is expressed as:

$$F_{y,i,Lin} \approx F_{y,i,Lin,0} + F'_{y,i,Lin,0}\left[\Delta F_{z,i} - \Delta F_{z,i,0}\right] \qquad (6)$$

where $F'_{y,i,Lin,0}$ is the lateral axle force gradient with respect to the load transfer, calculated at $\Delta F_{z,i,0}$. By combining (4)–(6), the lateral axle force is computed as:

$$F_{y,i} \approx F_{y,i,Lin,0} + F'_{y,i,Lin,0}\left[\Delta F_{z,i} - \Delta F_{z,i,0}\right]$$
$$+ \left[\alpha_i - \alpha_{i,0}\right]\left\{C_{i,0} + C'_{i,0}\left[\Delta F_{z,i} - \Delta F_{z,i,0}\right]\right\} \qquad (7)$$

B. Comparison With Conventional Axle Force Models (Model B and Model C)

The MF and Model A results are compared with those from the classic formulation in [8] and [25], called Model B in the remainder:

$$F_{y,i} \approx \alpha_i \left\{C_{1,i}\left[F_{z,i,L} + F_{z,i,R}\right] + C_{2,i}\left[F_{z,i,L}^2 + F_{z,i,R}^2\right]\right\} \qquad (8)$$

where $F_{z,i,L}$ and $F_{z,i,R}$ are the left and right vertical tire loads, including the respective load transfer; and C_1 and C_2 are constant parameters. For Model B, C_1 and C_2 were calculated by imposing the axle cornering stiffness at zero slip angle to be the same as for the MF at $\Delta F_{z,i,0}$ and $\Delta F_{z,i,0} + 500$ N. The latter condition is indicated with the subscript ILT, i.e., increased load transfer.

As the linearity of Model B with respect to slip angle does not allow to match the lateral force value of the MF for a generic $\alpha_{i,0}$, which represents a major drawback, a re-arranged version of (8) is included in the comparison, which is called Model C in

the remainder:

$$F_{y,i} \approx F_{y,i,Lin,0} + \left[\alpha_i - \alpha_{i,0}\right]\left\{C_{1,i}\left[F_{z,i,L} + F_{z,i,R}\right]\right.$$
$$\left. + C_{2,i}\left[F_{z,i,L}^2 + F_{z,i,R}^2\right]\right\} \qquad (9)$$

In (9) the cornering stiffness varies with the load transfer, similarly to (8), while $F_{y,i,Lin,0}$, i.e., the lateral axle force at the linearization point, is imposed. For Model C, C_1 and C_2 were calculated by imposing the axle cornering stiffness at $\alpha_{i,0}$ to be the same as for the MF at $\Delta F_{z,i,0}$ and $\Delta F_{z,i,0} + 500$ N.

Table I shows the model comparison for the front axle force of the case study 1 vehicle at three lateral accelerations, i.e., 3 m/s^2, 6 m/s^2 and 9 m/s^2, which are used as linearization points. The corresponding slip angles and load transfers were obtained at 100 km/h with the non-linear quasi-static model of Section V.

As expected, the MF, Model A and Model C output the same lateral axle force, $F_{y,F,0} = F_{y,F,Lin,0}$, for $(\alpha_{F,0}; \Delta F_{z,F,0})$, whilst this is not the case for Model B. To assess the situation when the slip angle and load transfer are varied, the parameter $\Delta F_{y,Mx,\Delta\alpha}$ is defined as:

$$\Delta F_{y,Mx,\Delta\alpha} = |F_{y,F,ILT,\Delta\alpha} - F_{y,F,\Delta\alpha}| \qquad (10)$$

where the notation Mx refers to the MF, Model A, Model B or Model C; and the subscript $\Delta\alpha = \alpha_F - \alpha_{F,0}$ indicates that the lateral force is calculated at $\alpha_{F,0} + \Delta\alpha$. For each model, $\Delta F_{y,Mx,\Delta\alpha}$ in (10) measures the effect of the load transfer on the lateral axle force at $\alpha_{F,0} + \Delta\alpha$. In fact, it is the effect of the input variations that matters in the frequency domain analyses. In particular, the percentage difference, $\Delta F_{y,\Delta\alpha,\%}$, of $\Delta F_{y,Mx,\Delta\alpha}$ for Models A-C (indicated by the subscripts A, B and C in (11)), with respect to the MF model, which is the reference model, is used as model accuracy performance indicator:

$$\Delta F_{y,\Delta\alpha,\%} = \left|\frac{\Delta F_{y,MF,\Delta\alpha} - \Delta F_{y,A/B/C,\Delta\alpha}}{\Delta F_{y,MF,\Delta\alpha}}\right| 100 \qquad (11)$$

The table reports the results for $\Delta\alpha = 0$ deg, -0.5 deg and 0.5 deg (see the last three columns on the right). In all cases, Model A provides significant benefit with respect to Model B and Model C. In fact, the deviations of Model A from the MF model range from 0% to ~12%, while they range from ~2% to ~168%
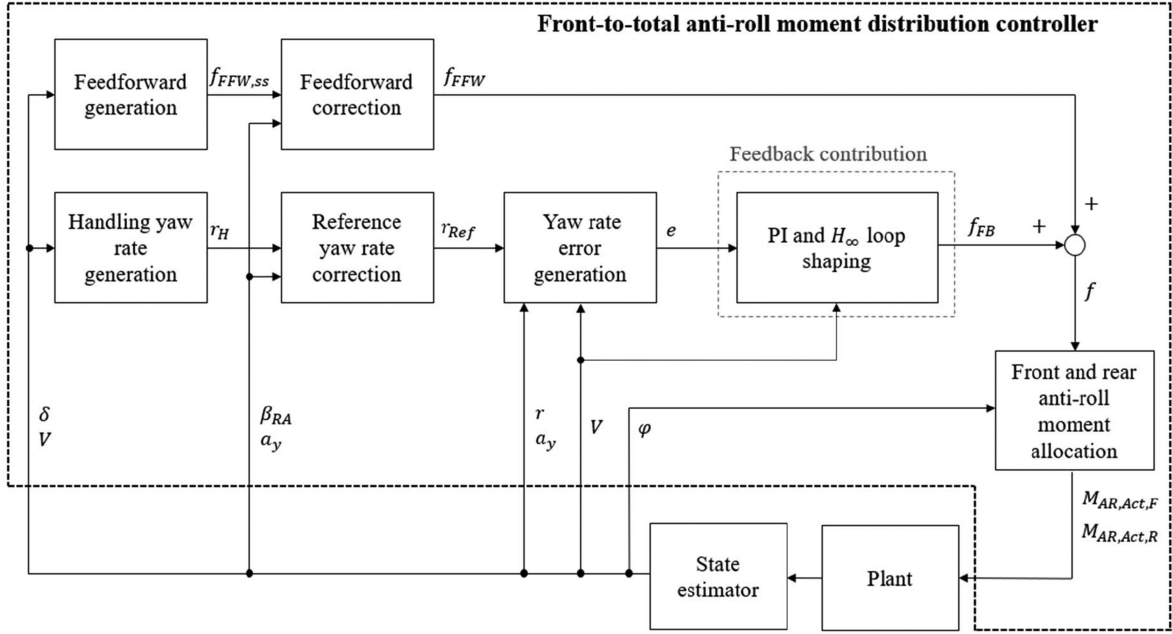
Fig. 6. Simplified schematic of the front-to-total anti-roll moment distribution control structure.

for Model B, and from ∼37% to 100% for Model C. Model B and Model C show a substantial performance decay with a_y, i.e., for large slip angles, which are the conditions of maximum effectiveness of the active suspension controller. The important conclusion is that Model B and Model C, differently from Model A, can be hardly considered reliable simplified models for anti-roll moment distribution control design.

IV. CONTROL STRUCTURE

Fig. 6 is the simplified schematic of the front-to-total anti-roll moment distribution control structure, consisting of: i) A static non-linear feedforward contribution generation block, based on steering input δ (average steering angle of the front wheels) and vehicle speed V; ii) A feedforward correction block, which provides appropriate dynamics to the feedforward contribution and deactivates it in specific conditions; iii) Blocks for the generation of the steady-state reference yaw rate for high tire-road friction conditions (handling yaw rate r_H) and its correction for transient and low tire-road friction conditions; iv) Blocks calculating control error e and the feedback control action f_{FB}; and v) An allocation algorithm for distributing the total active anti-roll moment between the front and rear axles based on the feedforward and feedback contributions as well as actuator limits, thus generating the anti-roll moment outputs $M_{AR,Act,F}$ and $M_{AR,Act,R}$. A state estimator provides the required variables, e.g., the estimated values of vehicle speed V, rear axle sideslip angle β_{RA}, and roll angle φ.

V. DESIGN OF REFERENCE VEHICLE BEHAVIOR AND STATIC NON-LINEAR FEEDFORWARD CONTRIBUTION

This section describes the quasi-static vehicle model based routine for the off-line design of the: i) Reference understeer characteristics; ii) Reference yaw rate maps; and iii) Static

non-linear feedforward anti-roll moment distribution ratio. This routine is an extension of the methodology presented in [48] for torque-vectoring system design.

A. Quasi-Static Vehicle Model

The quasi-static vehicle model has 8 degrees of freedom. The model consists of algebraic equations, which are solved through optimization functions, such as *fmincon* of Matlab, without forward time integration. The vehicle equations are used as equality constraints in an optimization problem. Hence, in the following the subscript "*dot*" indicates that the time derivative terms are dealt with as algebraic variables. The model is described by the following approximated force and moment balance equations (see also Fig. 7):

- Longitudinal force balance

$$m \left[V_{dot} \cos \beta - V \beta_{dot} \sin \beta - r V \sin \beta \right]$$

$$= -F_{drag} + \sum_{j=1}^{4} F_{x,j} \cos (\delta_j + \Delta \delta_j)$$

$$- \sum_{j=1}^{4} F_{y,j} \sin (\delta_j + \Delta \delta_j) \tag{12}$$

- Lateral force balance

$$m \left[V_{dot} \sin \beta + V \beta_{dot} \cos \beta + r V \cos \beta \right]$$

$$= \sum_{j=1}^{4} F_{x,j} \sin (\delta_j + \Delta \delta_j)$$
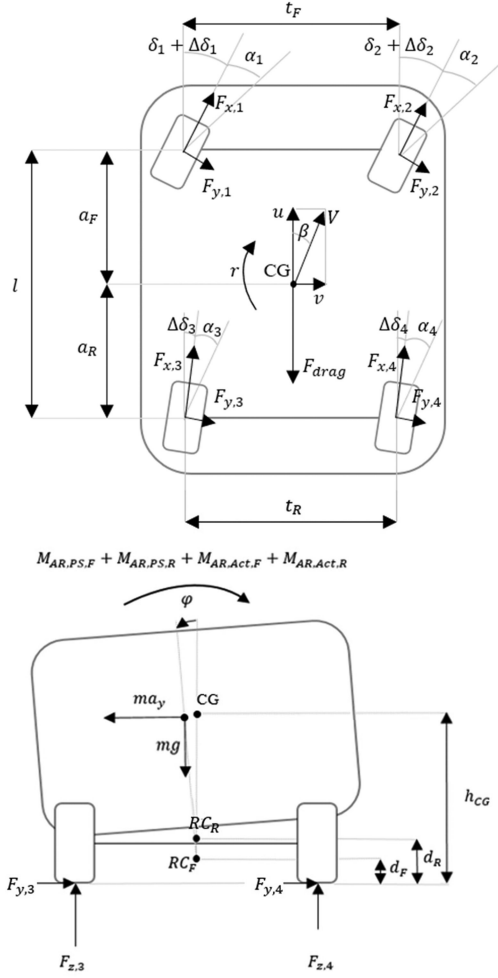
$$+ \sum_{j=1}^{4} F_{y,j} \cos (\delta_j + \Delta \delta_j) \tag{13}$$

Fig. 7. Top and rear views of the vehicle with indication of the main variables and parameters.

- Yaw moment balance

$$J_z r_{dot} = \sum_{j=1}^{4} M_{z,j}$$

$$+ \sum_{j=1}^{2} a_F \left[F_{x,j} \sin(\delta_j + \Delta\delta_j) + F_{y,j} \cos(\delta_j + \Delta\delta_j) \right]$$

$$- \sum_{j=3}^{4} a_R \left[F_{x,j} \sin(\Delta\delta_j) + F_{y,j} \cos(\Delta\delta_j) \right]$$

$$+ \frac{t_F}{2} \left[F_{x,1} \cos(\delta_1 + \Delta\delta_1) - F_{y,1} \sin(\delta_1 + \Delta\delta_1) \right]$$

$$- \frac{t_F}{2} \left[F_{x,2} \cos(\delta_2 + \Delta\delta_2) - F_{y,2} \sin(\delta_2 + \Delta\delta_2) \right]$$

$$+ \frac{t_R}{2} \left[F_{x,3} \cos(\Delta\delta_3) - F_{y,3} \sin(\Delta\delta_3) \right]$$

$$- \frac{t_R}{2} \left[F_{x,4} \cos(\Delta\delta_4) - F_{y,4} \sin(\Delta\delta_4) \right] \tag{14}$$

- Roll moment balance

$$J_x \varphi_{dot,dot} = m[V_{dot} \sin\beta + V\beta_{dot} \cos\beta$$
$$+ rV \cos\beta] [h_{CG} - d] \cos(\varphi)$$
$$+ mg [h_{CG} - d] \sin(\varphi)$$
$$- M_{AR,PS,F} - M_{AR,PS,R} - M_{AR,PD,F}$$
$$- M_{AR,PD,R} - M_{AR,Act,F}$$
$$- M_{AR,Act,R} \tag{15}$$

- j-th wheel moment balance

$$J_{w,j}\omega_{dot,j} = T_j - F_{x,j}R_{l,j} - M_{y,j} \tag{16}$$

where the angular acceleration of the j-th wheel is given by:

$$\omega_{dot,j} = \frac{V_{dot,x,j}}{R_{e,j}} [\sigma_{x,j} + 1] + \frac{V_{x,j}}{R_{e,j}} \sigma_{dot,x,j} \tag{17}$$

V is vehicle velocity, with longitudinal and lateral components u and v; β is the sideslip angle; r is the yaw rate; φ is the roll angle; J_z is the yaw mass moment of inertia of the vehicle; δ_j and $\Delta\delta_j$ are the steering angle and toe angle of the j-th tire (in the specific vehicle $\delta_3 = \delta_4 = 0$); $F_{x,j}$, $F_{y,j}$ and $M_{z,j}$ are the longitudinal force, lateral force and self-alignment moment of the j-th tire, evaluated through the MF, starting from the slip ratios and slip angles derived from kinematic equations (see the formulations in [46], [47]); F_{drag} is the aerodynamic drag force; J_x is the roll mass moment of inertia; RC_F and RC_R are the front and rear roll centers, with heights d_F and d_R; d is the distance between the center of gravity and the roll axis, calculated as the weighted average of d_F and d_R based on the longitudinal position of the center of gravity; g is the gravitational acceleration; h_{CG} is the center of gravity height; T_j is the wheel torque, which includes the driving and braking contributions; $R_{l,j}$ is the laden tire radius; $J_{w,j}$ is the wheel moment of inertia; $M_{y,j}$ is the rolling resistance torque; $R_{e,j}$ is the effective wheel radius; and $V_{dot,x,j}$ is the longitudinal acceleration of the j-th wheel center in the tire reference system. The model calculates the vertical loads according to the speed, and longitudinal and lateral acceleration levels [46], [47].

In this study steady-state conditions were imposed in (12)–(17), i.e., $V_{dot} = \beta_{dot} = \varphi_{dot} = \varphi_{dot,dot} = \sigma_{dot,x,j} = r_{dot} = 0$. β is considered small, which leads to $\cos\beta \approx 1$ and $\sin\beta \approx \beta$. This results in:

$$\begin{cases} a_x = V_{dot}\cos\beta - V\beta_{dot}\sin\beta - rV\sin\beta \approx -rV\beta \\ a_y = V_{dot}\sin\beta + V\beta_{dot}\cos\beta + rV\cos\beta \approx rV \end{cases} \tag{18}$$

where a_x is the longitudinal acceleration, and a_y is the lateral acceleration.

The optimization routine also includes inequality constraints, e.g., in terms of actuation and slip ratio limits (the latter to prevent wheel spinning or locking). The understeer characteristic of the vehicle without controller ('Passive' in Fig. 8) is obtained by imposing the constant baseline front-to-total roll anti-roll moment distribution, i.e., that of the passive suspension components, without using any cost function in the optimization.
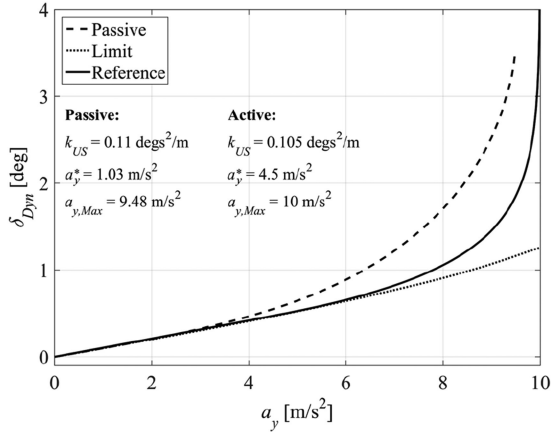
Fig. 8. Understeer characteristics of the passive vehicle (Passive), limit understeer characteristic (Limit), and reference understeer characteristic for the active vehicle (Reference).
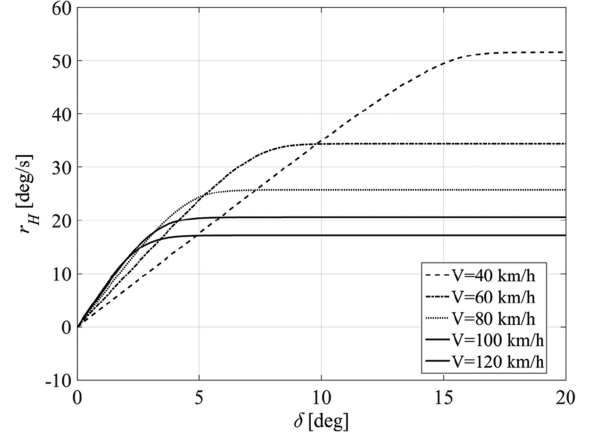

Fig. 9. Example of reference yaw rate map.
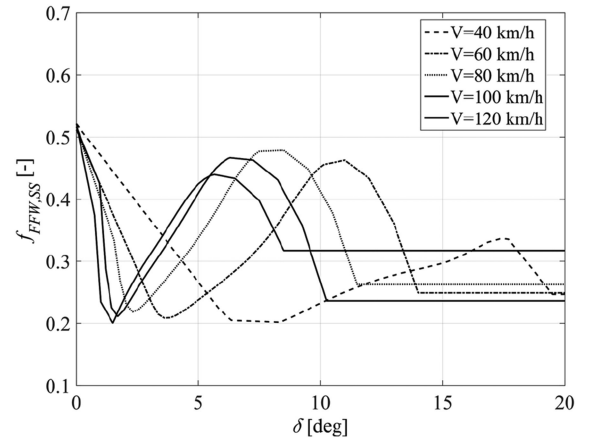
Fig. 10. Example of feedforward front-to-total anti-roll moment distribution map.

B. Design of Reference Cornering Response and Feedforward Distribution Ratio

The routine consists of the following steps:

Step 1: Minimization of the absolute value of the dynamic steering angle, $|\delta_{Dyn}|$, which is the cost function J of the optimization:

$$\min_{\arg f} (J) = \min_{\arg f} |\delta_{Dyn}|$$
$$= \min_{\arg f} |\delta - \delta_{Kin}| = \min_{\arg f} |\delta - lr/V| \qquad (19)$$

δ_{Dyn} is the difference between the average steering angle of the front wheels, δ, and the kinematic steering angle, δ_{Kin}. Hence, the optimization outputs the limit understeer characteristic ('Limit' in Fig. 8), i.e., the one that makes the vehicle as close as possible to the neutral steering behavior, together with the corresponding values of f, which is the front-to-total anti-roll moment distribution parameter for the active part of the anti-roll moment:

$$f = \frac{M_{AR,Act,F}}{M_{AR,Act,F} + M_{AR,Act,R}} \qquad (20)$$

Step 2: Selection of the reference understeer characteristic, $\delta_{Dyn,Ref}(a_y)$. Since the understeer characteristic from Step 1 is usually not suitable for a real-world application as the driver normally prefers some level of understeer to indicate when the cornering limit is approached, $\delta_{Dyn,Ref}(a_y)$ is selected to be intermediate between that of the passive vehicle and the limit one, through a graphical user interface overlapping the different characteristics. $\delta_{Dyn,Ref}(a_y)$ ('Reference' in Fig. 8) is approximated with a linear function up to the lateral acceleration a_y^*, and a logarithmic function for higher lateral accelerations [48]:

$$\delta_{Dyn,Ref} = \begin{cases} k_{US}a_y; & a_y < a_y^* \\ k_{US}a_y^* \\ \quad + \left[a_y^* - a_{y,Max} \right] k_{US} \\ \quad \times \log\left(\frac{a_y - a_{y,Max}}{a_y^* - a_{y,Max}} \right); & a_y \geq a_y^* \end{cases} \qquad (21)$$

where k_{US} is the understeer gradient in the linear part of the characteristic; and $a_{y,Max}$ is the maximum reference lateral acceleration. k_{US}, a_y^*, and $a_{y,Max}$ are user-defined parameters (examples of values are reported in Fig. 8).

Step 3: Recalculation of the reference understeer characteristic from Step 2 in terms of actual steering angle and vehicle speed, to obtain $\delta_{Ref}(a_y, V)$:

$$\delta_{Ref}(a_y, V) = \delta_{Dyn,Ref}(a_y) + \frac{l a_y}{V^2} \qquad (22)$$

Step 4: Calculation of the reference yaw rate characteristic. $\delta_{Ref}(a_y, V)$ from Step 3 is manipulated and interpolated to obtain the reference lateral acceleration characteristic, $a_{y,Ref}(\delta, V)$. The map of the steady-state reference yaw rate for high tire-road friction conditions (Fig. 9), called handling yaw rate in the remainder, is derived as $r_H(\delta, V) = a_{y,Ref}(\delta, V)/V$. r_H is the yaw rate that makes the vehicle follow the reference understeer characteristic.

Step 5: Design of the feedforward front-to-total distribution ratio, $f_{FFW,SS}$ (Fig. 10). $r_H(\delta, V)$ from Step 4 is imposed as a further equality constraint in the optimization, which is run without a cost function as the number of equality constraints is equal to the number of variables.

$f_{FFW,SS}(\delta, V)$, together with $r_H(\delta, V)$, is stored in look-up tables. Additional variables, such as the longitudinal acceleration or total torque demand, could be used as optimization parameters and map inputs, depending on the specific vehicle requirements. In the implementation of the controller, similarly to the reference yaw rate, $f_{FFW,SS}(\delta, V)$ is filtered through an appropriate first order transfer function, which outputs f_{FFW}. To prevent an undesired system response, a progressive deactivation algorithm of the feedforward contribution is present, which imposes f_{Nom}, i.e., the nominal front-to-total distribution of the passive vehicle (0.54 for case study 1 and 0.57 for case study 2), in case of significant absolute values of the yaw rate error e, or estimated rear axle sideslip angle $|\hat{\beta}_{RA}|$. Typical thresholds for e are those corresponding to the intervention of the stability control systems based on the actuation of the friction brakes.

VI. FEEDBACK CONTRIBUTION

A. Reference Yaw Rate and Yaw Rate Error

The feedback contribution uses a single input single output (SISO) formulation, aimed at tracking the reference yaw rate r_{Ref}. r_{Ref} is based on the steady-state value $r_{Ref,SS}$, which is the weighted sum of the handling yaw rate r_H and the stability yaw rate r_S. r_H represents the reference yaw rate for the vehicle operating in high tire-road friction conditions. r_S is a yaw rate that is compatible with the available tire-road friction conditions, i.e., with the current level of measured lateral acceleration a_y.

The stability yaw rate, r_S, is calculated from its saturation value r_{Sat}, which depends on a_y according to the steady-state relationship between yaw rate and lateral acceleration [49]:

$$r_{Sat} = \frac{a_y - \text{sign}(a_y) \Delta a_y}{V} \qquad (23)$$

The term Δa_y provides some conservativeness on r_{Sat}, i.e., to ensure that the vehicle with a yaw rate equal to r_{Sat} is actually operating within its cornering limit. In the practical tuning of the controller, Δa_y can be defined as a function of $|a_y|$. The stability yaw rate r_S is given by:

$$r_S = \begin{cases} r_H & \text{if } |r_H| < |r_{Sat}| \\ |r_{Sat}|\text{sign}(r_H) & \text{if } |r_H| \geq |r_{Sat}| \end{cases} \qquad (24)$$

Based on r_H and r_S, $r_{Ref, SS}$ is:

$$r_{Ref,SS} = r_H - W_\beta [r_H - r_S] = [1 - W_\beta] r_H + W_\beta r_S \qquad (25)$$

The weighting factor W_β is a linear function of $|\hat{\beta}_{RA}|$, which is used to determine the severity of the operating conditions of the vehicle. In critical maneuvers $\hat{\beta}_{RA}$ can be estimated with one of the methodologies from the literature, e.g., see [50]. W_β is saturated between 0 and 1:

$$W_\beta = \begin{cases} 0 & \text{if } \left|\hat{\beta}_{RA}\right| < \beta_{Act} \\ \frac{|\hat{\beta}_{RA}| - \beta_{Act}}{\beta_{Lim} - \beta_{Act}} & \text{if } \beta_{Act} \leq \left|\hat{\beta}_{RA}\right| \leq \beta_{Lim} \\ 1 & \text{if } \left|\hat{\beta}_{RA}\right| > \beta_{Lim} \end{cases} \qquad (26)$$

For large values of $|\hat{\beta}_{RA}|$ it is $r_{Ref,SS} = r_S$, whereas for small values of $|\hat{\beta}_{RA}|$ it is $r_{Ref,SS} = r_H$. The activation threshold

is β_{Act}, i.e., the value of $|\hat{\beta}_{RA}|$ below which no correction is applied to r_H. The limit threshold is β_{Lim}, i.e., the value of $|\hat{\beta}_{RA}|$ above which $r_{Ref,SS} = r_S$. The actual reference yaw rate, r_{Ref}, is generated by filtering $r_{Ref,SS}$ with a first order transfer function, typically fine-tuned based on the subjective feedback of test drivers (see also [51] for an analysis of the effect of such filter). β_{Act} and β_{Lim} do not have any influence in normal driving conditions, but they determine the cornering response when the vehicle is at or beyond the limit of handling. This conservative strategy can negatively affect vehicle performance in case of significant inaccuracy of the sideslip angle estimation.

The yaw rate error e used for the computation of the feedback contribution of the controller is given by:

$$e \approx W_V W_{a_y} [r - r_{Ref}] \text{sign}(\hat{\varphi})$$
$$\approx W_V W_{a_y} [r - r_{Ref}] \text{sign}(a_y) \qquad (27)$$

(27) must account for the fact that the effect of f depends on the direction of the vertical load transfer, or, if its precise estimate is not available, on the sign of roll angle or lateral acceleration. This justifies the inclusion of the sign of the estimated roll angle $\hat{\varphi}$ in (27), or alternatively, in a first approximation, of sign (a_y). The weights W_V and W_{a_y}, respectively functions of V and a_y, allow the progressive activation/deactivation of the feedback contribution at low speed and lateral acceleration.

B. Linearized Model for Control System Design

The linearized single-track model for control system design has 3 degrees of freedom. Its lateral force, yaw moment and roll moment balance equations are:

$$mV\left[\dot{\beta} + r\right] = F_{y,F} + F_{y,R} \qquad (28)$$

$$J_z \dot{r} = F_{y,F} a_F - F_{y,R} a_R + M_{z,Ext} \qquad (29)$$

$$J_x \ddot{\varphi} = mV[\dot{\beta} + r]h_{CG} + mgh_{CG}\varphi - [K_F + K_R]\varphi - [D_F + D_R]\dot{\varphi} - M_{AR,Act,F} - M_{AR,Act,R} \qquad (30)$$

where K_F and K_R are the front and rear roll stiffness of the passive suspension components, D_F and D_R are the front and rear roll damping of the passive components; $M_{z,Ext}$ is an external yaw moment contribution, for example from a torque-vectoring controller. The roll center is assumed to be at the road level.

The linearized model in (7), or alternatively (9), is used for the calculation of the lateral axle forces $F_{y,i}$ in (28)–(30). The lateral load transfer $\Delta F_{z,i}$ is calculated through a simplified version of (1):

$$\Delta F_{z,i} = \frac{K_i \varphi + D_i \dot{\varphi} + M_{AR,Act,i}}{t_i} \qquad (31)$$

The linearized expression of the slip angles, for small angle approximations, are:

$$\alpha_F = \beta + \frac{a_F r}{V} - \delta$$

$$\alpha_R = \beta - \frac{a_R r}{V} \qquad (32)$$

The active anti-roll moment contributions are calculated as:

$$M_{AR,Act,F} = f M_{AR,Act,Tot}$$
$$M_{AR,Act,R} = [1 - f] \, M_{AR,Act,Tot} \quad (33)$$

where $M_{AR,Act,Tot}$ is the total anti-roll moment caused by the active suspension system. The latter can be a function of the measured lateral acceleration or estimated roll angle and roll rate. In the specific linearized implementation, it is:

$$M_{AR,Act,Tot} = M_{AR,Act,Tot,0} + K_{Act,Tot} [\varphi - \varphi_0]$$
$$+ D_{Act,Tot} [\dot{\varphi} - \dot{\varphi}_0] \quad (34)$$

where $M_{AR,Act,Tot,0}$ is the anti-roll moment value at the linearization point, defined by φ_0 and $\dot{\varphi}_0$. $M_{AR,Act,Tot}$ is designed to significantly reduce the roll motion with respect to the passive vehicle without active suspension. $K_{Act,Tot}$ and $D_{Act,Tot}$ are the active parts of the total roll stiffness and roll damping of the vehicle.

By combining (7), or alternatively (9), with (28)–(34) and linearizing, the system is expressed in the following state-space form:

$$\dot{x} = Ax + Bu + Gd + E \quad (35)$$

where A, B, G and E are the system matrices; x is the state vector; u is the input vector; and d is the disturbance vector. The states, input and disturbances are:

$$x = \begin{bmatrix} \Delta\beta \\ \Delta r \\ \Delta\varphi \\ \Delta\dot{\varphi} \end{bmatrix} = \begin{bmatrix} \beta - \beta_0 \\ r - r_0 \\ \varphi - \varphi_0 \\ \dot{\varphi} - \dot{\varphi}_0 \end{bmatrix}, \; u = [\Delta f], \; d = \begin{bmatrix} \Delta\delta \\ \Delta M_{z,ext} \end{bmatrix}$$

$$(36)$$

The notation Δ indicates that the respective variable is given by the difference from its value in the linearization point, indicated by the subscript "0". E contains the constant terms resulting from the linearization. The values of the variables in the linearization points are provided by the combination of the quasi-static model of Section V and the linearized model for $\dot{x} = 0$. From (35) and (36), the vehicle transfer function relevant to the design of the front-to-total anti-roll moment distribution controller is $G_{Veh}(s) = \Delta r / \Delta f$, where s is the Laplace operator. A first order transfer function with a pure time delay, $G_{Act}(s)$, is used for modelling the dynamics of the specific actuators, which means that the plant transfer function, $G_{Plant}(s)$, is:

$$G_{Plant}(s) = \frac{\Delta r}{\Delta f}(s) \frac{e^{-T_{Act}s}}{\tau_{Act}s + 1} = G_{Veh}(s) G_{Act}(s) \quad (37)$$

where τ_{Act} and T_{Act} are the actuation system time constant and pure time delay.

C. PI and H_∞ Controller Design

The model of Section VI-B can be used for the design of any feedback control structure. For example, the implementations of this study are based on proportional integral (PI) control (case study 2), and an H_∞ loop shaping formulation with an observer/state feedback form [52] (case study 1). The latter was chosen for: i) Its robustness with respect to parametric

uncertainties, e.g., tire conditions, chassis compliance, vehicle inertia and actuator dynamics; ii) The fact that it is based on a conventional proportional integral (PI) formulation, which facilitates its industrial implementation; and iii) The fact that it allows gain scheduling, in this case with respect to V. The design process is based on two steps:

Step 1: Design of the PI controller gains. The PI control law in the time domain, $G_{PI}(t)$, is:

$$G_{PI}(t) = K_P(V) e(t) + \int K_I(V) e(t) dt$$
$$+ \int K_{AW}(V) \left[f_{Sat}(t^-) - f_{FFW}(t^-) \right.$$
$$\left. - f_{FB}(t^-) \right] dt \quad (38)$$

where t is time and t^- indicates the time at the previous time step; K_P, K_I and K_{AW} are the proportional, integral and anti-windup gains, which are scheduled with V; f_{FB} is the feedback contribution of the controller; and f_{Sat} is the saturated value of f, given by:

$$f_{Sat} = \text{sat}_{f_{Min}}^{f_{Max}}(f_{FB} + f_{FFW}) \quad (39)$$

where f_{Min} and f_{Max} are the minimum and maximum values of the distribution ratio, dynamically calculated as the more conservative option between: i) Distribution ratio limits based on actuator force limits, depending on the set-up and current operating conditions of the system; and ii) Fixed distribution thresholds defined a-priori during the control design stage.

The PI gains were selected through an optimization routine formulated as:

$$\min_{\arg K_P, K_I} (J_{PI}) = W_1 \bar{t}_{Rise} + W_2 \overline{O}$$
$$\text{s.t.} \; GM > GM_{Thrs}$$
$$PM > PM_{Thrs} \quad (40)$$

where J_{PI} is the cost function, which is minimized through the Matlab *pattern search* function [53]; W_1 and W_2 are weighting factors, set to 0.15 and 1; $\bar{t}_{Rise}$ and $\overline{O}$ are the normalized rise time and overshoot of the closed-loop system, with normalization values equal to 0.10 s and 20%; and GM and PM are the gain and phase margins, which must be larger than the threshold values GM_{Thrs} and PM_{Thrs}, respectively set to 2 and 30 deg [52]. The optimization in (40) was repeated for different values of V, which is a relatively slowly varying parameter. Despite the non-linearity of (27), in the controller design the system model is linearized around a specific cornering condition, and therefore it is assumed that the sign of the lateral acceleration a_y does not change, which makes the feedback system linear. The PI controller design is complete at the end of Step 1.

Step 2: H_∞ loop shaping design [52]. The shaped plant is defined as a function of V:

$$G_s(V) = G_{PI}(V) G_{Plant}(V) G_{PC}(V) = \begin{bmatrix} A_s(V) & B_s(V) \\ C_s(V) & 0 \end{bmatrix}$$
$$(41)$$

where $G_{PC}(V)$ is the post-compensator and $A_s(V)$, $B_s(V)$ and $C_s(V)$ are the matrices of the state-space formulation of

TABLE II
EXAMPLE OF FEEDBACK CONTROLLER GAINS, STABILITY AND ROBUSTNESS INDICATORS, CASE STUDY 1, $V = 100$ km/h

a_y [m/s^2]	$K_{P,A}$ [s/rad]	$K_{I,A}$ [1/rad]	$K_{P,C}$ [s/rad]	$K_{I,C}$ [1/rad]	$GM_{A/A}$ [-]	$GM_{C/A}$ [-]	$PM_{A/A}$ [deg]	$PM_{C/A}$ [deg]	Stability A/A	Stability C/A	$\varepsilon_{Max,A/A,PI}$ [-]	$\varepsilon_{Max,A/A,H_\infty}$ [-]
3	160.32	503.40	81.80	266.16	2.00	3.93	37.99	81.18	Yes	Yes	0.29	0.55
6	14.85	99.95	6.54	10.13	2.01	5.16	32.96	94.87	Yes	Yes	0.28	0.54
9	3.81	9.27	-5.91	-7.75	2.80	27.81	46.94	-150.27	Yes	No	0.22	0.51

the shaped plant. The system transfer function, $G_{Plant}(V)$, is thus augmented by a pre-compensator $G_{PI}(V)$, and post-compensator, which is a diagonal matrix used to achieve the desired value of stability margin. The observer/state feedback form for H_∞ loop shaping control is obtained according to [52] and [51], the latter referring to a very similar vehicle yaw rate tracking problem.

D. Analysis of the Axle Force Formulation Effect

The PI controller gains were designed according to Step 1 of Section VI-C, by using: i) The linearized vehicle model of Section VI-B, including the Model A formulation for the lateral axle forces (see (7)), and providing the gains $K_{P,A}$ and $K_{I,A}$ in Table II; and ii) The same linearized vehicle model as in i), this time adopting Model C of Section III-B for the lateral axle forces, which corresponds to the gains $K_{P,C}$ and $K_{I,C}$.

Table II shows an example of comparison of the PI gains obtained from the two models of the case study 1 vehicle at three lateral accelerations, i.e., 3 m/s^2, 6 m/s^2 and 9 m/s^2, together with the respective gain margins ($GM_{A/A}$ and $GM_{C/A}$) and phase margins ($PM_{A/A}$ and $PM_{C/A}$), and the indication on whether the closed-loop system is stable (Stability A/A and Stability C/A), based on its eigenvalues. The first letter in the subscript of the margin notations indicates the lateral axle force model used for the PI gain calculation (Model A or Model C), while the second letter indicates the model adopted for the margin calculation, i.e., Model A in all cases, as this is the higher fidelity model.

The PI gains obtained from the two models are significantly different for all a_y values. In particular, at 3 m/s^2 and 6 m/s^2, in which the increase of the lateral load transfer brings a reduction of both cornering stiffness and lateral axle force, Model C implies a conservative selection of the gains. More importantly, at 9 m/s^2 Model C compromises system stability. In fact, in such condition the front axle cornering stiffness increases with the load transfer, while the lateral axle force decreases, where the latter is the prevalent effect. Based on the cornering stiffness variation, Model C brings negative values of $K_{P,C}$ and $K_{I,C}$, while $K_{P,A}$ and $K_{I,A}$ are positive. Simulations with the non-linear model for control system assessment (the one used in Section VII-A) confirmed the instability of the controller design based on Model C at 9 m/s^2.

During the analysis, it was also verified that the controller based on Model A at 9 m/s^2 meets the gain and phase margin specifications for the entire range of a_y. Therefore, the on-line implementation uses only the gains calculated for 9 m/s^2, while it includes gain scheduling with V, i.e., the controller parameters are implemented in the form look-up tables that are functions of vehicle speed. It was not considered beneficial to vary the gains

TABLE III
MAIN VEHICLE PARAMETERS

Parameter	Description	Value
m	Vehicle mass	2530 kg
J_z	Yaw mass moment of inertia	3500 kg m^2
a_F	Front semi-wheelbase	1.559 m
a_R	Rear semi-wheelbase	1.374 m
h_{CG}	Center of gravity height	0.72 m
t_F	Front track width	1.676 m
t_R	Rear track width	1.742 m
f_{Nom}	Static anti-roll moment distribution ratio of the passive suspension components	0.54

with respect to such a swiftly changing variable as a_y, to prevent stability issues.

The values of the maximum robust stability margins for the PI and H_∞ controllers at 9 m/s^2 (the lateral acceleration used in the controller implementation), respectively $\varepsilon_{Max,A/A,PI}$ and $\varepsilon_{Max,A/A,H_\infty}$ in Table II, (see [52] for the definition of ε_{Max}), show the robustness benefit of the H_∞ formulation.

VII. RESULTS

A. Case Study 1: Simulations of a Vehicle With Active Anti-Roll Bars

Case study 1 is an electric SUV with front and rear active anti-roll bars, which is simulated with an experimentally validated non-linear Matlab-Simulink model, with the same degrees of freedom as the quasi-static model of Section V.

The main vehicle parameters are in Table III. Fig. 11 reports examples of validation results of the passive vehicle, in terms of: i) Understeer and sideslip angle characteristics (Fig. 11(a) and Fig. 11(b)) during a skidpad test; and ii) Time histories of steering wheel angle (Fig. 11(c)), lateral acceleration (Fig. 11(d)) and yaw rate (Fig. 11(e)) during an obstacle avoidance test from 65 km/h. Given the good match between simulations and experiments, the model can be considered a reliable tool for controller assessment.

The passive vehicle, i.e., the vehicle without active anti-roll bars nor stability control actuated through the friction brakes, is compared with the same vehicle with the suspension controller of this study, including the feedforward and feedback contributions (the latter with the H_∞ loop shaping controller). In case study 1 the feedback contribution was subject to a progressive activation with vehicle speed and lateral acceleration, according to W_V and W_{a_y} in (27).

Fig. 12 refers to a ramp steer maneuver at 100 km/h, i.e., with a steering wheel input applied with a slow ramp. The dynamic
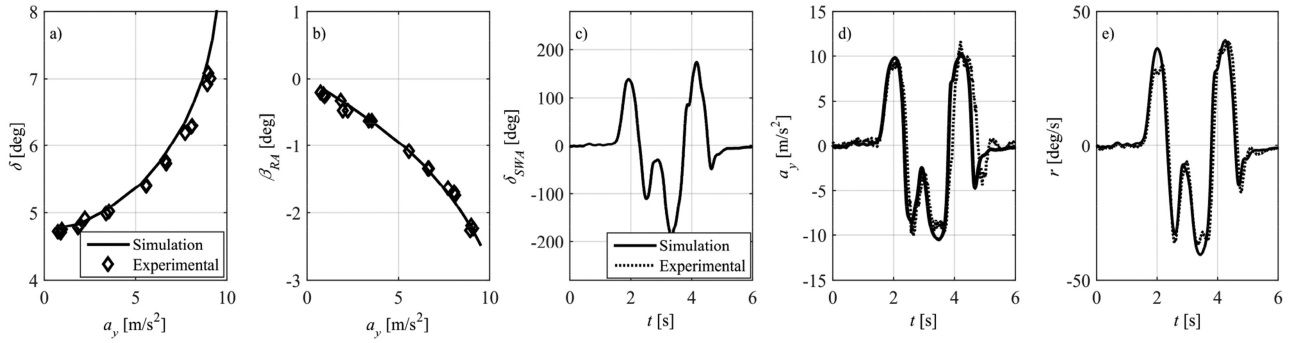
Fig. 11.   Case study 1: non-linear model validation results.
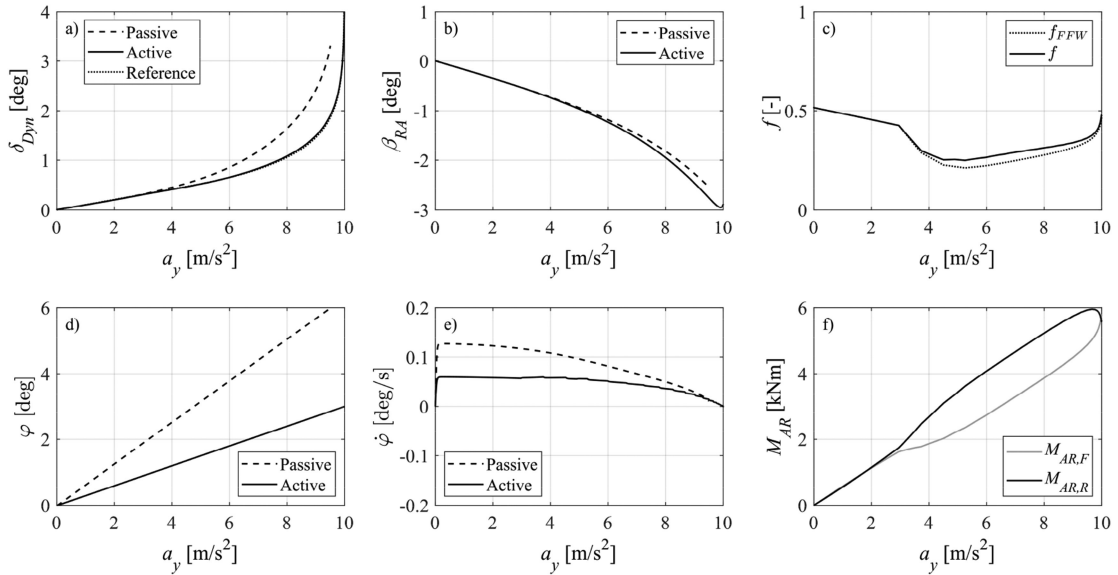

Fig. 12.   Case study 1: ramp steer simulation results in high friction conditions.

steering angle (Fig. 12(a)), rear axle sideslip angle (Fig. 12(b)), front-to-total anti-roll moment distribution ratio (Fig. 12(c)), roll angle (Fig. 12(d)), roll rate (Fig. 12(e)), and total front and rear anti-roll moments (Fig. 12(f)) are plotted as functions of a_y.

The active vehicle closely follows the reference understeer characteristic, which is less understeering than the one of the passive vehicle, has a wider linear region, and is characterized by a 4.6% increase of the maximum lateral acceleration, i.e., from 9.56 m/s^2 to 10.00 m/s^2. This is achieved through a front-to-total ratio of the active part of the anti-roll moment, which is significantly lower ($\sim$0.25 at 5 m/s^2) than that ($\sim$0.54) of the passive suspension components.

Because of the approximately steady-state nature of the maneuver, most of the control effort is associated with the feedforward contribution, while the feedback contribution is almost inactive. As a result of the additional active anti-roll moment of the active system, the roll angle is approximately halved.

Fig. 13 reports the time histories of the main variables during the simulation of a multiple step steer from an initial speed of 100 km/h, in high tire-road friction conditions. Immediately before the steering wheel input, the electric motor torque demand is set to 0 and the vehicle is coasting at progressively

decreasing speed. The first steering wheel application varies the steering wheel angle from 0 deg to 150 deg (the steering ratio is $\sim$15); the second application changes the steering wheel angle from 150 deg to -150 deg; and the final application brings the angle back to 0 deg. The steering wheel rate of each application is 400 deg/s. The higher speed values than in Fig. 11, with the associated reduced value of yaw damping, tend to excite important yaw rate and sideslip angle oscillations in the passive vehicle. The yaw rate and sideslip angle of the controlled car exhibit significant reductions of their overshoots and oscillations with respect to the passive vehicle. For example, the first yaw rate peak decreases from $\sim$34 deg/s to $\sim$28 deg/s, and the first yaw rate undershoot is fully compensated by the controller. The peak value of $|\beta_{RA}|$ decreases from $\sim$7 deg for the passive vehicle, to $\sim$3.5 deg for the active one, which does not even require the intervention of the sideslip contribution. In terms of tracking performance, the root mean square value of $r - r_{Ref}$ is $\sim$1.1 deg/s for the controlled vehicle, which is nearly a 50% reduction with respect to the $\sim$2.1 deg/s of the passive vehicle. As expected, in the transient part of the maneuver the intervention of the feedback contribution is prevalent over the non-linear feedforward contribution.
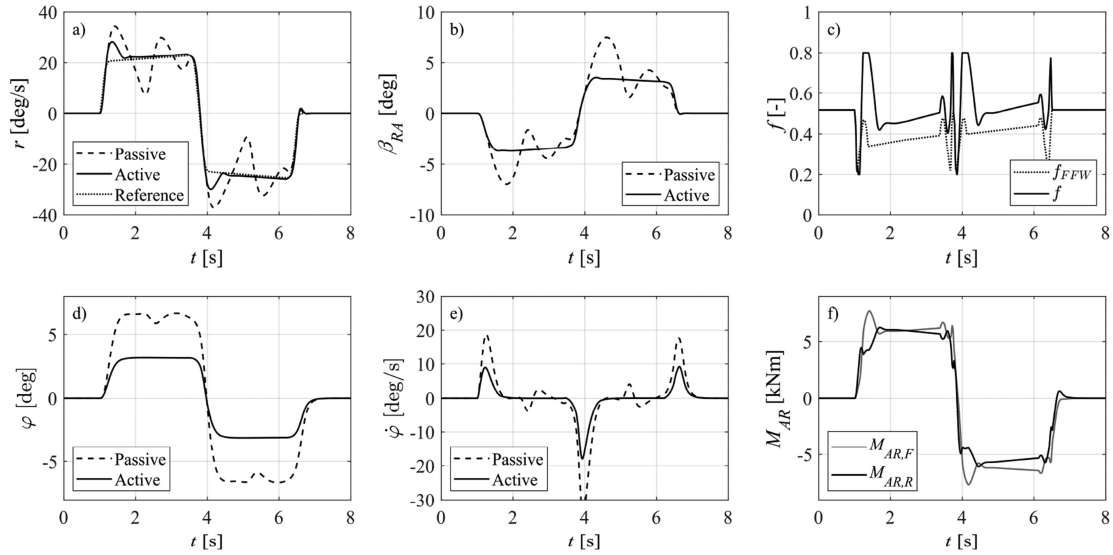
Fig. 13. Case study 1: multiple step steer simulation results in high friction conditions.
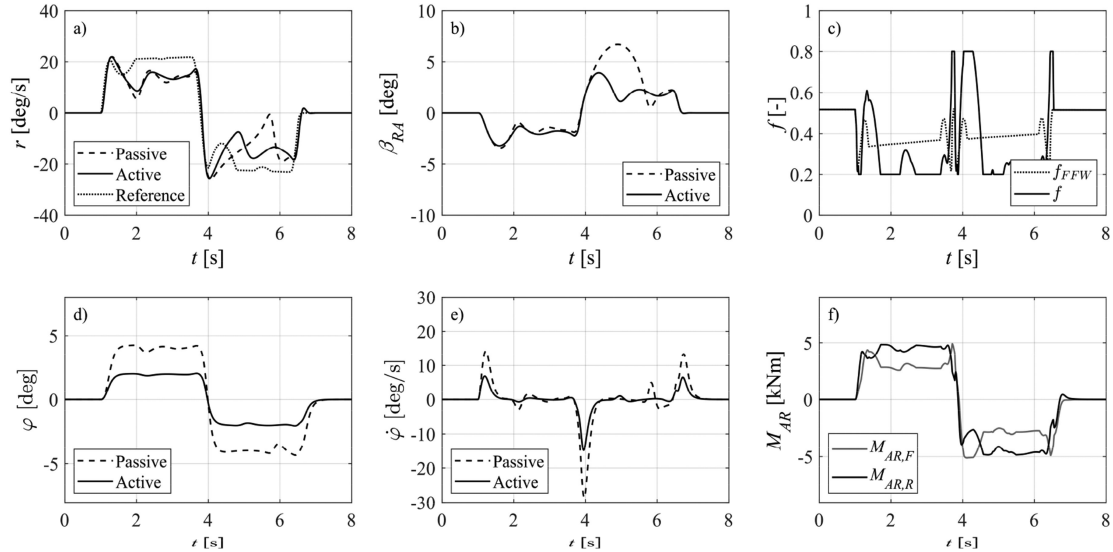

Fig. 14. Case study 1: multiple step steer simulation results in low friction conditions.

When the car settles and reaches the steady-state condition, the feedforward component of the controller becomes dominant again. Also in this test, the roll angle (Fig. 13(d)) and the roll rate (Fig. 13(e)) are reduced.

Fig. 14 reports multiple step steer simulation results for a tire-road friction coefficient $\mu = 0.6$, from an initial speed $V = 100$ km/h. Even though the effectiveness of the variable anti-roll moment distribution is limited by the modest levels of lateral acceleration and load transfer, the controller reduces the yaw rate oscillations (Fig. 14(a)) and the peak values of the rear axle sideslip angle (Fig. 14(b)), especially after the second steering application.

To evaluate the controller effectiveness in closed-loop tests with a path tracking driver model based on feedforward and feedback contributions (see [54] for the details of the path tracking algorithm), Fig. 15 shows the results for an obstacle avoidance

test from an initial speed of 71 km/h, in high tire-road friction conditions. The suspension controller facilitates the return of the vehicle to its original path (Fig. 15(b)), with significantly reduced control effort in terms of steering angle (Fig. 15(a)). Also, the controlled vehicle experiences lower peak values of the yaw rate r and rear axle sideslip angle β_{RA} with respect the passive one, which is hardly controllable by a normal driver (with a peak value of $|\beta_{RA}|$ of $\sim$25 deg, see Fig. 15(d)). The significant controller benefits are objectively assessed in Table IV, based on the following performance indicators (defined in [54]): i) The root mean square value of the lateral position error at the center of gravity, $RMS_{\Delta y_{CG}}$; ii) The root mean square value of the heading angle error, $RMS_{\Delta \psi_{CG}}$, between the center of gravity trajectory and the reference path; iii) The root mean square value of the rear axle sideslip angle, $RMS_{\beta_{RA}}$; iv) The maximum absolute value of the rear axle sideslip angle, $|\beta_{RA,Max}|$; and v)
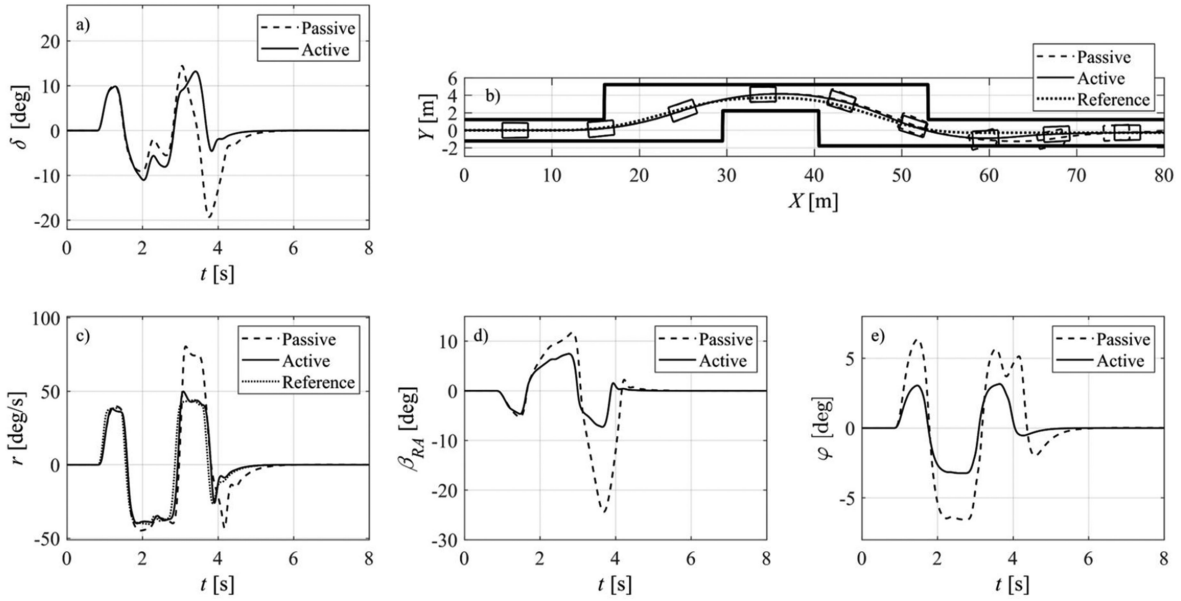
Fig. 15.   Case study 1: obstacle avoidance simulation results in high friction conditions.

TABLE IV
MAIN RELEVANT PERFORMANCE INDICATORS FOR THE OBSTACLE
AVOIDANCE MANEUVER

	$RMS_{\Delta y_{CG}}$ [m]	$RMS_{\Delta \psi_{CG}}$ [deg]	$RMS_{\beta_{RA}}$ [deg]	$|\beta_{RA,Max}|$ [deg]	$IACA_\delta$ [deg]
Passive	0.40	6.63	7.99	24.39	4.38
Active	0.26	2.87	3.41	7.09	3.69

Fig. 16.   Case study 2: the SUV demonstrator during the experimental session at the Lommel proving ground (Belgium).

The integral of the absolute value of the steering angle, $IACA_\delta$, normalized with time.

B. Case Study 2: Preliminary Experiments on a Vehicle With Active Suspension Actuators

The feedforward and feedback controller was preliminarily assessed on a second SUV demonstrator (Fig. 16), equipped with a production hydraulic active suspension system – the Tenneco Monroe intelligent suspension, ACOCAR. At each vehicle corner, a pump pressurizes the hydraulic circuit of the respective actuator and inputs energy into the system. The pressure level

in the hydraulic chambers is modulated through the currents of the base and piston valves of the actuator, which is installed in parallel to an air spring. Depending on the operating conditions, the time constant of the hydraulic actuators ranges from 25 ms to 60 ms, with a pure time delay of approximately 15 ms.

A centralized skyhook algorithm and roll angle compensation controller, already installed and tested on the case study SUV, were integrated with the front-to-total anti-roll moment distribution controller. For ease of implementation, in case study 2 the feedback contribution included only the PI terms, with $W_{a_y} = 1$, i.e., the feedback contribution was not subject to deactivation with lateral acceleration. The controller was implemented with two driving modes: i) The Normal mode, providing an understeer characteristic rather similar to that of the vehicle without the anti-roll moment distribution controller; and ii) The Sport mode, significantly reducing the level of vehicle understeer in steady-state cornering.

During the experiments, the stability controller based on the actuation of the friction brakes was deactivated, to prevent interferences. In this case the so-called baseline configuration, used as term of comparison, is the same vehicle demonstrator, including the pre-existing skyhook and roll angle compensation algorithms, but excluding the anti-roll moment distribution controller.

The experimental results of skidpad and step steer tests are reported in Figs. 17–19, and confirm the analysis of case study 1. In fact, during the skidpad in Sport mode the SUV is substantially neutral steering up to a lateral acceleration of ~7 m/s², after which it understeers, to make the driver perceive that the cornering limit is approached. The maximum lateral acceleration of the active vehicle is 9.50 m/s², which is a >10% improvement with respect to the 8.55 m/s² of the baseline configuration. Fig. 17 also reports the f contributions (f and f_{FFW}), as well as the corresponding actuation forces, $F_{Act,1}$ and $F_{Act,3}$ (see Fig. 7 for the numbering conventions), on the outer corners. As expected,
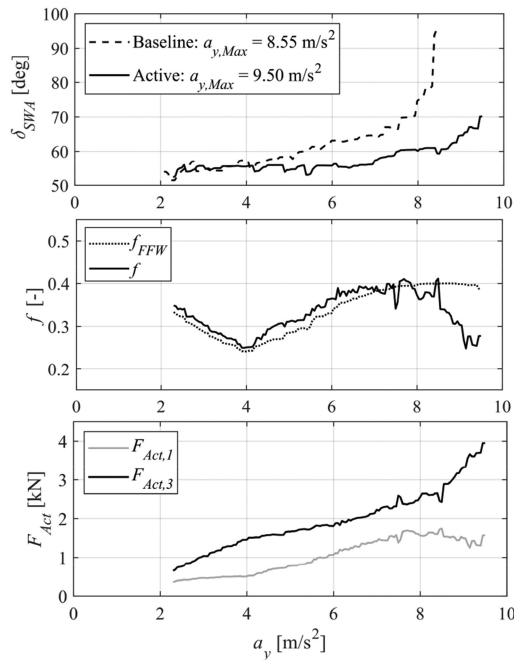
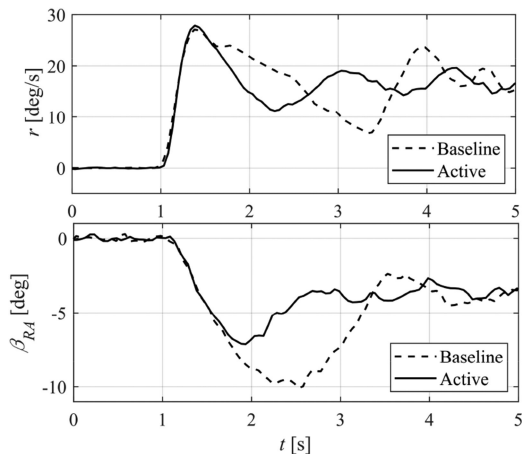Fig. 17. Case study 2: experimental skidpad results (Sport mode).

Fig. 18. Case study 2: experimental step steer results (Normal mode).
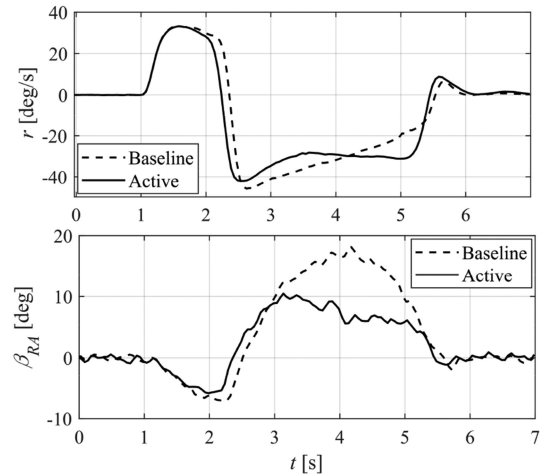

Fig. 19. Case study 2: experimental multiple step steer results (Normal mode).

second steering wheel input is applied, and tends to destabilize the vehicle, which reaches a sideslip angle peak of ∼18 deg in baseline configuration, against the only ∼10 deg of the active case. Such benefit is achieved through the activation of the sideslip contribution of the reference yaw rate.

VIII. CONCLUSION

This study presented a methodology, based on a non-linear quasi-static model and a linearized single-track vehicle model, for the design of the feedforward and feedback contributions of an anti-roll moment distribution controller for vehicles with active suspensions. The analysis led to the following conclusions:

- The lateral load transfer between the two tires of the same axle always causes a reduction of the lateral axle force; however, for the considered sets of tire parameters (see Section II), at medium-high slip angles the load transfer also provokes a cornering stiffness increase, which is a novel observation, with important control design implications.
- The proposed linearized model for control system design accounts for the variations of the lateral axle force and cornering stiffness in the linearization point, as functions of the lateral load transfer, as discussed in Section III. The comparison with the magic formula model shows a decisive performance improvement of the novel lateral axle force model with respect to the conventional linearized formulation from the literature, especially at high lateral accelerations, as reported in Table I.
- Differently from the conventional formulation, the novel linearized model allows stable design of the feedback contribution for the whole lateral acceleration range (see Table II in Section VI).
- The adopted reference yaw rate formulation, described in Section VI, permits the implementation of continuous yaw rate control with an indirect constraint on sideslip angle, while maintaining a simple and versatile control structure, which can be used with any SISO controller.

the feedforward contribution is responsible for the majority of the control effort during the skidpad.

The step steer of Fig. 18, from an initial speed of 110 km/h and with a steering wheel amplitude of 90 deg, highlights the functionality of the sideslip-based correction of the reference yaw rate in (23)–(26), with β_{Act} and β_{Lim} of 6.5 deg and 9 deg. Such correction is responsible for the yaw rate decrease between 1.5 s and 2.5 s. The result is that the sideslip angle peak is reduced by the controller, while its steady-state value is approximately the same as for the baseline configuration. The multiple step steer test of Fig. 19, from an initial speed of 65 km/h and with a 150 deg amplitude of the steering wheel inputs, confirms the effectiveness of the controller during swift variations of the load transfer direction. In fact, after 2 s, the

- The offline optimization routine for the design of the reference understeer characteristics and feedforward anti-roll moment distribution reduces the feedback control effort in most driving conditions, as shown in Figs. 12(c) and 17 in Section VII, and allows a conservative design of the feedback control contribution, which attenuates the potential comfort and drivability issues associated with sensor noise.
- The controller was assessed on two applications, i.e., through simulations of a vehicle with active anti-roll bars (case study 1) and experiments on a vehicle with hydraulic suspension actuators on each corner (case study 2). The results show the controller capability of achieving apparently opposite objectives, such as: i) Shaping the vehicle understeer characteristic, with less understeer in steady-state cornering and substantial increase of the maximum achievable lateral acceleration ($>4\%$ for case study 1, see Fig. 12(a), and $>10\%$ for case study 2, see Fig. 17); and ii) Reducing yaw rate and sideslip oscillations in extreme transient conditions, see Fig. 13(a) and Figs. 18–19.

The next steps will include a careful subjective assessment of the control system performance, and the integration of anti-roll moment distribution control with brake-based stability control systems and torque-vectoring controllers.

REFERENCES

[1] A. van Zanten, R. Erhardt, G. Pfaff, "VDC, the vehicle dynamics control system of Bosch," SAE, Warrendale, PA, USA, Tech. Paper 950749, 1995.

[2] A. van Zanten, "Bosch ESP systems: 5 years of experience," SAE, Warrendale, PA, USA, Tech. Paper 2000-01-1633, 2000.

[3] L. De Novellis et al., "Direct yaw moment control actuated through electric drivetrains and friction brakes: Theoretical design and experimental assessment," Mechatronics, vol. 26, pp. 1–15, 2015.

[4] L. De Novellis, A. Sorniotti, and P. Gruber, "Driving modes for designing the cornering response of fully electric vehicles with multiple motors," Mech. Syst. Signal Process., vol. 64–65, pp. 1–15, 2015.

[5] Q. Lu et al., "Enhancing vehicle cornering limit through yaw rate and sideslip control," Mech. Syst. Signal Process., vol. 75, pp. 455–472, 2016.

[6] M. Nagai, Y. Hirano, and S. Yamanaka, "Integrated control of active rear wheel steering and direct yaw moment control," Vehicle Syst. Dyn., vol. 27, no. 5, pp. 357–370, 1997.

[7] M. Abe, "A study on effects of roll moment distribution control in active suspension on improvement of limit performance of vehicle handling," Int. J. Vehicle Des., vol. 15, no. 3–5, pp. 326–336, 1994.

[8] D. E. Williams and W. M. Haddad, "Nonlinear control of roll moment distribution to influence vehicle yaw characteristics," IEEE Trans. Control Syst. Technol., vol. 3, no. 1, pp. 110–116, Mar. 1995.

[9] J. Gerhard, M. C. Laiou, M. Monnigmann, and W. Marquardt, "Robust yaw control design with active differential and active roll control systems," IFAC Proc., vol. 38, no. 1, pp. 73–78, 2005.

[10] P. H. Cronjé and P. S. Els, "Improving off-road vehicle handling using an active anti-roll bar," J. Terramechanics, vol. 47, no. 3, pp. 179–189, 2010.

[11] D. Cimba, J. Wagner, and A. Baviskar, "Investigation of active torsion bar actuator configurations to reduce vehicle body roll," Vehicle Syst. Dyn., vol. 44, no. 9, pp. 719–736, 2006.

[12] K. N. Kota and B. Sivanandham, "Integrated model-in-loop (MiL) simulation approach to validate active roll control system," SAE, Warrendale, PA, USA, Tech. Paper 2017-01-0435, 2017.

[13] M. O. Bodie and A. Hac, "Closed loop yaw control of vehicles using magneto-rheological dampers," SAE, Warrendale, PA, USA, Tech. Paper 2000-01-0107, 2000.

[14] D. E. Williams and W. M. Haddad, "Active suspension control to improve vehicle ride and handling," Int. J. Vehicle Mechanics Mobility, vol. 28, no. 1, pp. 1–24, 1997.

[15] M. Lakehal-Ayat, S. Diop, and E. Fenaux, "An improved active suspension yaw rate control," in Proc. Amer. Control Conf., 2002, pp. 863–868.

[16] A. Sorniotti and N. D'Alfio, "Vehicle dynamics simulation to develop an active roll control system," SAE, Warrendale, PA, USA, Tech. Paper 2007-01-0828, 2007.

[17] D. Danesin, P. Krief, A. Sorniotti, and M. Velardocchia, "Active roll control to increase handling and comfort," SAE, Warrendale, PA, USA, Tech. Paper 2003-01-0962, 2003.

[18] M. Coric, J. Deur, J. Kasac, and H. E. Tseng, "Optimisation of active suspension control inputs for improved vehicle handling performance," Vehicle Syst. Dyn., vol. 54, no. 11, pp. 1574–1600, 2016.

[19] K. Shimada and Y. Shibahata, "Comparison of three active chassis control methods for stabilizing yaw moments," SAE, Warrendale, PA, USA, Tech. Paper 940870, 1994.

[20] A. Hac and M. O. Bodie, "Improvements in vehicle handling through integrated control of chassis systems," Int. J. Vehicle Auton. Syst., vol. 1, no. 1, pp. 83–110, 2002.

[21] S. Ikenaga, F. L. Lewis, J. Campos, and L. Davis, "Active suspension control of ground vehicle based on a full-vehicle model," in Proc. Amer. Control Conf., 2000, pp. 4019–4024.

[22] N. Zulkarnain, F. Imaduddin, H. Zamzuru, and S. A. Mazlan, "Application of an active anti-roll bar system for enhancing vehicle ride and handling," in Proc. IEEE Colloq. Humanities, Sci. Eng., 2012, pp. 260–265.

[23] K. Hudha and Z. A. Kadir, "Modelling, validation and roll moment rejection control of pneumatically actuated active roll control for improving vehicle lateral dynamics performance," Int. J. Eng. Syst. Modelling Simul., vol. 1, no. 2/3, pp. 122–136, 2009.

[24] N. Cooper, D. Crolla, and M. Levesley, "Integration of active suspension and active driveline to ensure stability while improving vehicle dynamics," SAE, Warrendale, PA, USA, Tech. Paper 2005-01-0414, 2005.

[25] D. J. M. Sampson and D. Cebon, "Active roll control of single unit heavy road vehicles," Vehicle Syst. Dyn., vol. 40, no. 4, pp. 229–270, 2003.

[26] S. M. Hwang and Y. Park, "Active roll moment distribution based on predictive control," Int. J. Vehicle Des., vol. 16, no. 1, pp. 15–28, 1995.

[27] S. Yim, K. Jeon, and K. Yi, "An investigation into vehicle rollover prevention by coordinated control of active anti-roll bar and electronic stability program," Int. J. Control, Autom. Syst., vol. 10, no. 2, pp. 275–287, 2012.

[28] J. Wang and S. Shen, "Integrated vehicle ride control via active suspensions," Int. J. Vehicle Mechanics Mobility, vol. 46, no. 1, pp. 495–508, 2008.

[29] J. Wang, D. A. Wilson, W. Xu, and D. A. Crolla, "Active suspension control to improve vehicle ride and steady-state handling," in Proc. Eur. Control Conf. IEEE Conf. Decis. Control, 2005, pp. 1982–1987.

[30] S. Yim, "Design of preview controllers for active roll stabilization," J. Mech. Sci. Technol., vol. 32, no. 4, pp. 1805–1813, 2018.

[31] K. Jeon, H. Hwang, S. Choi, J. Kim, K. Jang, and K. Yi, "Development of an electric active roll control (ARC) algorithm for a SUV," Int. J. Automot. Technol., vol. 13, no. 2, pp. 247–253, 2012.

[32] D. Li, S. Du, and F. Yu, "Integrated vehicle chassis control based on direct yaw moment, active steering and active stabilizer," Int. J. Vehicle Mechanics Mobility, vol. 46, no. 1, pp. 341–351, 2008.

[33] S. Yim and K. Yi, "Design of an active roll control system for hybrid four-wheel-drive vehicles," Proc. Institution Mech. Eng., D J. Automobile Eng., vol. 227, no. 2, pp. 151–163, 2013.

[34] H. Her, J. Suh, and K. Yi, "Integrated control of the differential braking, the suspension damping force and the active roll moment for improvement in the agility and the stability," Proc. Institution Mech. Eng., D J. Automobile Eng., vol. 229, no. 9, pp. 1145–1157, 2015.

[35] F. Gay, N. Coudert, and I. Rifqi, "Development of hydraulic active suspension with feedforward and feedback design," SAE, Warrendale, PA, USA, Tech. Paper 2000-01-0104, 2000.

[36] M. Yamamoto, "Active control strategy for improved handling and stability," SAE, Warrendale, PA, USA, Tech. Paper 911902, 1991.

[37] Y. A. Ghoneim, "Active roll control and integration with electronic stability control system: Simulation study," Int. J. Vehicle Des., vol. 56, no. 1–4, pp. 317–340, 2011.

[38] P. Serrier, X. Moreau, and A. Oustaloup, "Active roll control device for vehicles equipped with hydropneumatic suspensions," IFAC Proc., vol. 39, no. 16, pp. 384–390, 2006.

[39] Y. Xu and M. Ahmadian, "Improving the capacity of tire normal force via variable stiffness and damping suspension system," J. Terramechanics, vol. 50, no. 2, pp. 122–132, 2013.

[40] C. March and T. Shim, "Integrated control of suspension and front steering to enhance vehicle handling," Proc. Institution Mech. Eng., D J. Automobile Eng., vol. 221, no. 4, pp. 377–391, 2007.

[41] D. Pi, X. Wang, H. Wang, and Z. Kong, "Development of hierarchical control logic for 2-channel hydraulic active roll control system," *ASME J. Dyn. Syst., Meas. Control*, vol. 140, no. 10, 2018, Art. no. 101009.

[42] K. Zhen-Xing, P. Da-Wei, C. Shan, W. Hong-Liang, and W. Xian-Hui, "Design and simulation of hierarchical control algorithm for electric active stabilizer bar system," in *Proc. Control Decision Conf.*, 2016, pp. 6069–6074.

[43] H. Sun, Y. H. Chen, H. Zhao, and S. Zhen, "Optimal design for robust control parameter for active roll control system: A fuzzy approach," *J. Vibration Control*, vol. 24, no. 19, pp. 4575–4591, 2017.

[44] T. Xinpeng and D. Xiaocheng, "Simulation and study of active roll control for SUV based on fuzzy PID," SAE, Warrendale, PA, USA, Tech. Paper 2007-01-3570, 2007.

[45] H. Pacejka, *Tyre and Vehicle Dynamics*, 3rd ed. Amsterdam, The Netherlands: Elsevier, 2012.

[46] W. F. Milliken and D. L. Milliken, *Race Car Vehicle Dynamics*, 1st ed. Warrendale, PA, USA: SAE Int., 1995.

[47] G. Genta, *Motor Vehicle Dynamics: Modeling and Simulation* (Series on Advances in Mathematics for Applied Sciences 43), 1st ed. Singapore: World Scientific, 1997.

[48] L. De Novellis, A. Sorniotti, and P. Gruber, "Wheel torque distribution criteria for electric vehicles with torque-vectoring differentials," *IEEE Trans. Veh. Technol.*, vol. 63, no. 4, pp. 1593–1602, 2014.

[49] B. Lenzo, A. Sorniotti, P. Gruber, and K. Sannen, "On the experimental analysis of single input single output control of yaw rate and sideslip angle," *Int. J. Automot. Technol.*, vol. 18, no. 5, pp. 799–811, 2017.

[50] S. Antonov, A. Fehn, and A. Kugi, "Unscented Kalman filter for vehicle state estimation," *Vehicle Syst. Dyn.*, vol. 49, no. 11, pp. 1497–1520, 2011.

[51] Q. Lu, A. Sorniotti, P. Gruber, J. Theunissen, J. De Smet, "H_∞ loop shaping for the torque vectoring control of electric vehicles: Theoretical design and experimental assessment," *Mechatronics*, vol. 35, pp. 32–43, 2016.

[52] S. Skogestad and I. Postlethwaite, *Multivariable Feedback Control: Analysis and Design*, 2nd ed. Hoboken, NJ, USA: Wiley, 2007.

[53] C. Audet and J. E. Dennis, "Analysis of generalized pattern searches," *SIAM J. Optim.*, vol. 13, no. 3, pp. 889–903, 2003.

[54] C. Chatzikomis, A. Sorniotti, P. Gruber, M. Zanchetta, D. Willans, and B. Balcombe, "Comparison of path tracking and torque-vectoring controllers for autonomous electric vehicles," *IEEE Trans. Intell. Vehicles*, vol. 3, no. 4, pp. 559–570, 2018.